

# Stratified tidal flow over a tall ridge above and below the turning latitude

R. C. Musgrave<sup>1,†</sup>, R. Pinkel<sup>1</sup>, J. A. MacKinnon<sup>1</sup>, Matthew R. Mazloff<sup>1</sup> and W. R. Young<sup>1</sup>

<sup>1</sup>Scripps Institution of Oceanography, University of California San Diego, CA 92037, USA

(Received 6 May 2015; revised 30 November 2015; accepted 18 February 2016;  
first published online 29 March 2016)

The interaction of the barotropic tide with a tall, two-dimensional ridge is examined analytically and numerically at latitudes where the tide is subinertial, and contrasted to when the tide is superinertial. When the tide is subinertial, the energy density associated with the response grows with latitude as both the oscillatory along-ridge flow and near-ridge isopycnal displacement become large. Where  $f \neq 0$ , nonlinear processes lead to the formation of along-ridge jets, which become faster at high latitudes. Dissipation and mixing is larger, and peaks later in the tidal cycle when the tide is subinertial compared with when the tide is superinertial. Mixing occurs mainly on the flanks of the topography in both cases, though a superinertial tide may additionally generate mixing above topography arising from convective breaking of radiating waves.

**Key words:** internal waves, mixing and dispersion, topographic effects

---

## 1. Introduction

The ubiquity of internal tides in the ocean has prompted extensive study of their generation at topography, and subsequent radiation (Bell 1975; Baines 1982; Llewellyn Smith & Young 2003). Their role in mixing the stably stratified ocean as they dissipate is well established (Munk & Wunsch 1998), and global climate models (GCMs) have provided insight into the remarkable sensitivity of large-scale ocean circulation on the distribution and magnitude of the mixing (Hasumi & Sugimoto 1999; Simmons *et al.* 2004; Jayne 2009). As a result, significant effort has been expended developing physically based parameterizations for dissipative processes associated with the superinertial internal tide, i.e. tidal motions with a period of less than one pendulum day (Green & Nycander 2013). These parameterizations are now being implemented in GCMs that are used to inform climate policy (e.g. Melet *et al.* 2013). In contrast, the mixing associated with subinertial tidal constituents is much less well studied and remains unaccounted for, despite large losses from the subinertial barotropic tide (Egbert & Ray 2003; Müller 2013).

On a traditional  $f$ -plane, the internal wave dispersion relation disallows radiating internal waves whose period is longer than that of the local pendulum day, which

<sup>†</sup>Present address: Massachusetts Institute of Technology, Cambridge, MA 02139-4307, USA.  
Email address for correspondence: [rmusg@mit.edu](mailto:rmusg@mit.edu)

means that subinertial tidal constituents do not generate radiating internal tides polewards of their turning latitudes (defined as where the tidal frequency matches the local Coriolis frequency, and sometimes called a critical latitude). The inclusion of ‘non-traditional’ Coriolis effects extends this latitudinal range by tens to hundreds of kilometres, depending on stratification, enabling subinertial waves to propagate over a limited range (Gerkema & Shrira 2005). However, in regions polewards of this, subinertial tides generate a baroclinic response that is evanescent, decaying exponentially away from topography. Globally these subinertial evanescent tides account for less baroclinic energy than their superinertial radiating counterparts, whose energy forms one of the dominant internal signals in the ocean. Nevertheless, observational and regional modelling studies indicate that the nearfield mixing associated with these trapped tides may be significant (Nakamura *et al.* 2000, 2010; Osafune & Yasuda 2013; Musgrave *et al.* 2016). To understand the role played by tidal dissipation poleward of the turning latitude, it is necessary to have an understanding of both the linear evanescent response and the typical nonlinear responses that arise. In this paper we present an idealized study that explores in detail the nature of the baroclinic response to subinertial tidal forcing at topography, and contrast the physics and processes leading to mixing to those in the relatively well-understood superinertial case.

In the first part of the paper we build on the work of Llewellyn Smith & Young (2003), to derive an analytic solution for subinertial trapped tides generated at a tall, infinitely thin ridge. We show that the baroclinic response is evanescent with a decay scale that decreases with increasing latitude. Both the along-ridge velocity and the near-ridge isopycnal displacement of the evanescent response grow with latitude away from the turning latitude. As a result, for a constant-amplitude barotropic tide, the total near-ridge energy density (i.e. kinetic plus potential) of the subinertial baroclinic response grows with latitude, in direct contrast with the superinertial baroclinic response which has a constant energy density at all latitudes.

We explore and verify these predictions in a series of idealized two-dimensional numerical simulations where a 24 h oscillating tide interacts with a Gaussian ridge at a range of latitudes. Of particular interest is the influence of latitude on the processes leading to turbulence. In the two-dimensional simulations presented here, we use mixing as a proxy for turbulence in the three-dimensional ocean. By performing ‘equivalent’ simulations at superinertial and subinertial latitudes, we find that transient hydraulic jumps are the dominant mechanism for mixing in our simulations when the tide is subinertial, and tidal lee waves formed from radiating constituents are additionally important when the tide is superinertial.

We also investigate the generation of tidally rectified along-ridge currents, whose energy is significant in the nearfield and increases with latitude. These have been examined analytically for both unstratified tidal flows (Huthnance 1973; Loder 1980), and stratified tidal flows over weak topography (Maas & Zimmerman 1989*b*; Brink 2011). The combination of tall topography and stratification places our simulations beyond the parameter regime of prior theory, but nevertheless we find similar qualitative results of strong along-slope flows, and weaker cross-slope and vertical circulations in the Eulerian time mean. An explicit calculation of particle paths show that particles near the ridge-crest undergo looping trajectories along the flanks for  $f \neq 0$ .

Observations of enhanced subinertial frequency currents around topography have motivated the investigation of trapped topographic waves (Rhines 1970; Chapman 1989; Brink 1990; Padman *et al.* 1992; Codiga 1997). These arise from a resonance

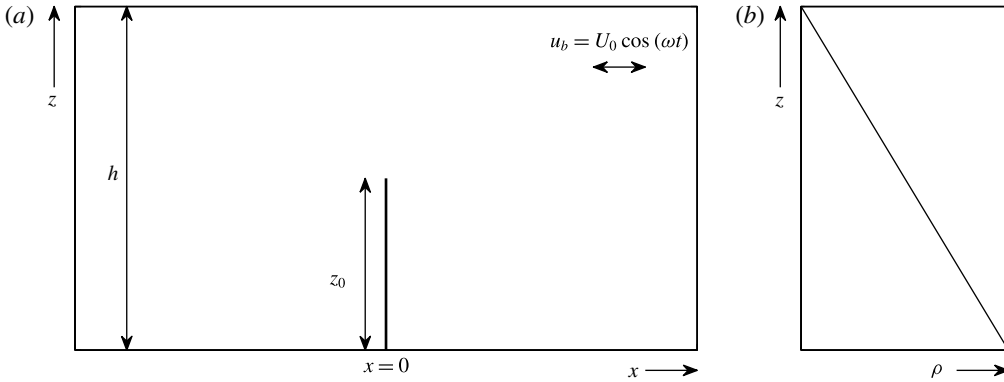


FIGURE 1. Definition sketch. (a) The barotropic tide oscillates over a tall, narrow ridge. (b) Density,  $\rho$ , increases uniformly with depth.

between the free modes associated with a certain topography and background stratification, and an ambient forcing frequency. The solutions presented in this paper are complementary, describing the forced response to subinertial tides which may be expected even in the absence of a resonance. When the forced response projects onto the free modes of a certain topography, a trapped wave may be resonantly generated.

The remainder of this paper is broadly divided into four parts: the first presents theoretical results for subinertial tidal forcing of a stratified fluid over a knife-edge ridge; the second presents a series of numerical experiments over a tall, narrow Gaussian ridge aimed at verifying the theory, and extending the description to larger amplitude, more nonlinear tides; and the third discusses the relevance of this work to more general three-dimensional situations. In the fourth section we present a summary.

## 2. Theory

In this section we extend the results of Llewellyn Smith & Young (2003) (hereafter LSY03) to include subinertial tidal forcings. A similar solution for superinertial tides at a knife edge is presented by St Laurent *et al.* (2003). The problem is formulated in two dimensions on an  $f$ -plane, with an imposed barotropic tide ( $u_b = U_0 \cos \omega t$ ) oscillating in the  $x$ -direction. The total fluid depth is  $h$ . At  $x = 0$  the tide interacts with an infinitely thin ridge of height  $z_0$ , where  $z_0 < h$  (figure 1). For simplicity we consider only uniform stratification ( $N$ ) in this study, though LSY03 additionally presents solutions for the case of slowly varying  $N(z)$ . The linearized equations are

$$\left. \begin{aligned} u_t - fv &= -p_x, \\ v_t + fu &= 0, \\ p_z &= b, \\ b_t + N^2 w &= 0, \\ u_x + w_z &= 0, \end{aligned} \right\} \quad (2.1)$$

where velocities are  $(u, v, w)$ , pressure is  $p$  and the Coriolis frequency is  $f$ . The density,  $\rho$ , has been written in terms of the Brunt–Väisälä frequency,  $N$ , and the

buoyancy,  $b$ :

$$\rho = \rho_0 \left[ 1 - \frac{N^2 z}{g} - \frac{b}{g} \right], \tag{2.2}$$

and pressure has been scaled by  $\rho_0$ . Defining a stream function  $(u, w) = (-\psi_z, \psi_x)$ , the equations can be combined, and written as

$$\psi_{zztt} + f^2 \psi_{zz} + N^2 \psi_{xx} = 0. \tag{2.3}$$

Imposing a boundary condition of no-flow through the barrier means

$$\psi(x = 0, z < z_0) = U_0 z \cos(\omega t), \tag{2.4}$$

such that  $U_T = u_b + u = U_0 \cos(\omega t) + u = 0$  on the knife-edge ridge.

In the linear limit we look for solutions which are time periodic at the tidal frequency,  $\omega$ :

$$\psi = U_0 \text{Re}\{e^{-i\omega t} \phi\}. \tag{2.5}$$

Then, equation (2.3) can be written

$$N^2 \phi_{xx} = (\omega^2 - f^2) \phi_{zz}, \tag{2.6}$$

with boundary conditions  $\phi(x = 0, z < z_0) = z$ , and  $\phi(x, h) = 0$ . For superinertial flows,  $\omega^2 > f^2$  and the equation is hyperbolic, however, for subinertial flows,  $\omega^2 < f^2$  and the equation is elliptic. The solution is constructed from an infinite sum of the vertical normal modes, defined by

$$\frac{d^2 a_n}{dz^2} + \frac{N^2 a_n}{c_n^2} = 0, \tag{2.7}$$

with  $a_n(0) = a_n(h) = 0$ , and  $\int_0^h a_n(z) a_m(z) dz = (h/2) \delta_{mn}$ . A Green's function solution to (2.6) satisfies

$$N^2 G_{xx} - (\omega^2 - f^2) G_{zz} = G_0 \delta(x) \delta(z - z'), \tag{2.8}$$

for a point source located at  $x = 0, z = z'$ . The normalization  $G_0$  will be determined shortly for convenience. We write the vertical dependence of the separable solution in terms of an infinite sum of vertical normal modes,  $a_n = \sin(nZ)$ ,

$$G(x, Z, Z') = \sum_{n=1}^{\infty} G_n(x, Z') \sin(nZ), \tag{2.9}$$

where  $Z = (\pi z)/h$ . For modal phase speeds  $c_n = hN/n\pi$ , we define two real wave numbers corresponding to the superinertial ( $\checkmark$ : below the turning latitude) and subinertial ( $\hat{\checkmark}$ : above the turning latitude) cases:

$$\checkmark k_n^2 = \frac{\omega^2 - f^2}{c_n^2} \quad \text{and} \quad \hat{\checkmark} k_n^2 = \frac{f^2 - \omega^2}{c_n^2}. \tag{2.10a,b}$$

The superinertial case is explicitly dealt with in LSY03, so here we concentrate on the subinertial case, for which (2.8) can be written in terms of vertical modes

$$\frac{\partial^2 \hat{G}_n}{\partial x^2} - \hat{\checkmark} k_n^2 \hat{G}_n = \frac{2}{h} G_0 \delta(x) \sin(nZ'). \tag{2.11}$$

For  $x \neq 0$ , the solution is

$$\hat{G}_n = A(z')e^{-\hat{k}_n|x|} = \begin{cases} Ae^{-\hat{k}_n x}, & x > 0 \\ Ae^{\hat{k}_n x}, & x < 0, \end{cases} \quad (2.12)$$

The constant,  $A$ , is determined by integrating (2.11) between  $x^- < 0$  and  $x^+ > 0$  and matching solutions as  $x \rightarrow 0$ , giving

$$A = -\frac{G_0}{\hat{k}_n h} \sin(nZ'). \quad (2.13)$$

The subinertial Green's function solution is

$$\hat{G} = -\frac{G_0}{h} \sum_{n=1}^{\infty} \frac{1}{\hat{k}_n} e^{-\hat{k}_n|x|} \sin(nZ') \sin(nZ). \quad (2.14)$$

For comparison, LSY03 equation (3.8) is the superinertial Green's Function solution

$$\check{G} = \frac{G_0}{h} \sum_{n=1}^{\infty} \frac{1}{i\check{k}_n} e^{i\check{k}_n|x|} \sin(nZ') \sin(nZ). \quad (2.15)$$

For consistency with LSY03, we define

$$\left. \begin{aligned} \check{\mu} &= \frac{N}{\sqrt{\omega^2 - f^2}}; & \check{k}_n &= \frac{n\pi}{h\check{\mu}}, \\ \hat{\mu} &= \frac{N}{\sqrt{f^2 - \omega^2}}; & \hat{k}_n &= \frac{n\pi}{h\hat{\mu}} \end{aligned} \right\} \quad (2.16)$$

and we non-dimensionalize  $X = \pi x / \mu h$ . Defining  $G_0 = -N^2 / \mu$  we write

$$\hat{G}(X, Z, Z') = \sum_{n=1}^{\infty} \frac{e^{-n|\hat{X}|}}{n\pi} \sin(nZ) \sin(nZ'), \quad (2.17)$$

to be compared with LSY03 equation (3.11) for the superinertial case:

$$\check{G}(X, Z, Z') = \sum_{n=1}^{\infty} \frac{e^{in|\check{X}|}}{n\pi} \sin(nZ) \sin(nZ'). \quad (2.18)$$

The series in (2.17) can be expressed using the real function

$$\bowtie(X, Z, Z') = \frac{\cos(Z + Z') - \cosh |X|}{\cos(Z - Z') - \cosh |X|} \quad (2.19)$$

and the Green's function becomes

$$\hat{G}(X, Z, Z') = \frac{\ln |\bowtie|}{4\pi}. \quad (2.20)$$

2.1. Streamfunction

The subinertial solution to (2.6) is represented in terms of the Green's function as

$$\hat{\phi}(X, Z) = \frac{h}{\pi} \int_0^{Z_0} \Gamma(Z') \hat{G}(X, Z, Z') dZ', \tag{2.21}$$

where  $Z_0 = \pi z_0/h$ , and  $\Gamma(Z')$  is the source density. Evaluated on the knife edge where the boundary condition is  $\phi(0, z < z_0) = z$ , this becomes

$$Z = \frac{1}{2\pi} \int_0^{Z_0} \Gamma(Z') \ln \left| \frac{\sin(\frac{1}{2}(Z + Z'))}{\sin(\frac{1}{2}(Z - Z'))} \right| dZ'. \tag{2.22}$$

LSY03 demonstrate this may be arranged to a standard form and solved for  $\Gamma$ :

$$\Gamma(Z) = 2\sqrt{\frac{1 - \cos(Z)}{\cos(Z) - \cos(Z_0)}}. \tag{2.23}$$

Substituting (2.17) and (2.23) into (2.21), and using the identity

$$\frac{2}{\pi} \int_0^{Z_0} \sin nZ \sqrt{\frac{1 - \cos(Z)}{\cos(Z) - \cos(Z_0)}} dZ = P_{n-1}(\cos Z_0) - P_n(\cos Z_0) \equiv PP_n, \tag{2.24}$$

where  $P_n$  is the  $n$ th Legendre polynomial, gives an expression for the streamfunction, which decays exponentially with distance away from the ridge:

$$\hat{\phi}(X, Z) = \frac{h}{\pi} \sum_{n=1}^{\infty} \frac{e^{-n|\hat{X}|}}{n} PP_n \sin(nZ). \tag{2.25}$$

For comparison, LSY03 gives the super inertial solution:

$$\check{\phi}(X, Z) = \frac{h}{\pi} \sum_{n=1}^{\infty} \frac{e^{in|\check{X}|}}{n} PP_n \sin(nZ). \tag{2.26}$$

2.2. Explicit fields and relative phases

The general streamfunction,  $\psi$ , may be written

$$\begin{aligned} \psi &= U_0 Re(e^{-i\omega t} \phi) \\ &= U_0 \phi_r \cos(\omega t) + U_0 \phi_i \sin(\omega t). \end{aligned} \tag{2.27}$$

Two components of the velocity field are directly evaluated from the streamfunction:  $(u, w) = (-\psi_z, \psi_x)$ . The remaining fields are derived from (2.1). The superinertial

fields are

$$\check{u} = -U_0 \sum_{n=1}^{\infty} PP_n \cos(nZ) \cos(n|\check{X}| - \omega t), \quad (2.28a)$$

$$\check{v} = -\frac{fU_0}{\omega} \sum_{n=1}^{\infty} PP_n \cos(nZ) \sin(n|\check{X}| - \omega t), \quad (2.28b)$$

$$\check{w} = -\text{sgn}(x) \frac{U_0}{\check{\mu}} \sum_{n=1}^{\infty} PP_n \sin(nZ) \sin(n|\check{X}| - \omega t), \quad (2.28c)$$

$$\check{b} = \text{sgn}(x) \frac{N^2 U_0}{\omega \check{\mu}} \sum_{n=1}^{\infty} PP_n \sin(nZ) \cos(n|\check{X}| - \omega t), \quad (2.28d)$$

$$\check{p} = -\text{sgn}(x) \frac{N^2 U_0 h}{\pi \omega \check{\mu}} \sum_{n=1}^{\infty} \frac{PP_n}{n} \cos(nZ) \cos(n|\check{X}| - \omega t). \quad (2.28e)$$

The subinertial fields are

$$\hat{u} = -U_0 \cos(\omega t) \sum_{n=1}^{\infty} e^{-n|\hat{X}|} PP_n \cos(nZ), \quad (2.29a)$$

$$\hat{v} = \frac{fU_0}{\omega} \sin(\omega t) \sum_{n=1}^{\infty} e^{-n|\hat{X}|} PP_n \cos(nZ), \quad (2.29b)$$

$$\hat{w} = -U_0 \cos(\omega t) \frac{\text{sgn}x}{\hat{\mu}} \sum_{n=1}^{\infty} e^{-n|\hat{X}|} PP_n \sin(nZ), \quad (2.29c)$$

$$\hat{b} = \frac{N^2 U_0}{\omega \hat{\mu}} \text{sgn}(x) \sin(\omega t) \sum_{n=1}^{\infty} e^{-n|\hat{X}|} PP_n \sin(nZ), \quad (2.29d)$$

$$\hat{p} = -\frac{N^2 U_0 h}{\pi \omega \hat{\mu}} \text{sgn}(x) \sin(\omega t) \sum_{n=1}^{\infty} \frac{e^{-n|\hat{X}|}}{n} PP_n \cos(nZ). \quad (2.29e)$$

Some important properties of the solutions are apparent by inspection, and are illustrated in figure 2, where we set  $U_0 = 0.006 \text{ m s}^{-1}$  and  $N = 0.0017 \text{ rad s}^{-1}$ . Subinertial solutions are evanescent and trapped to the ridge crest with a decay scale  $1/\hat{k}$  that decreases with latitude. Superinertial solutions are radiating waves with wavenumbers  $\check{k}$ , and form characteristic internal wave beams at slopes determined by the dispersion relation. At  $x=0$  the subinertial buoyancy field has a quadrature phase relationship with the barotropic tide, indicating that the largest isopycnals at the ridge occur during slack tide. Conversely, the superinertial buoyancy field is in phase, and peak isopycnal displacements are associated with peak cross-ridge flows.

### 2.3. Energetics

Using the expressions obtained in the previous section, we evaluate the time and depth mean kinetic and potential energy at the ridge-crest ( $x=0$ ) using the following

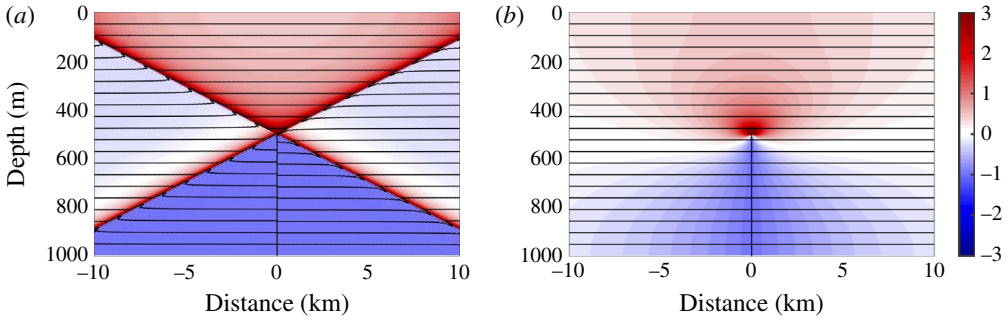


FIGURE 2. Horizontal velocities non-dimensionalized by  $U_0$  (colour) and isopycnals (contours) at  $t = 0$  for (a) superinertial ( $f_{10^\circ}$ ) and (b) subinertial ( $f_{50^\circ}$ ) solutions.

definitions appropriate for hydrostatic dynamics:

$$\left. \begin{aligned} \overline{\text{KE}} &= \frac{\rho_0}{2} \frac{1}{Th} \int_0^T \int_0^h (u^2 + v^2) \, dz \, dt, \\ \overline{\text{APE}} &= \frac{\rho_0}{2N^2} \frac{1}{Th} \int_0^T \int_0^h b^2 \, dz \, dt. \end{aligned} \right\} \quad (2.30)$$

The integrals are evaluated over the full water depth, capturing the energy associated with the response on the flank of the ridge as well as above its crest. The superinertial energies are

$$\left. \begin{aligned} \check{\overline{\text{KE}}} &= \frac{1}{8} \rho_0 U_0^2 \left( \frac{\omega^2 + f^2}{\omega^2} \right) \sum_{n=1}^{\infty} PP_n^2, \\ \check{\overline{\text{APE}}} &= \frac{1}{8} \rho_0 U_0^2 \left( \frac{\omega^2 - f^2}{\omega^2} \right) \sum_{n=1}^{\infty} PP_n^2, \end{aligned} \right\} \quad (2.31)$$

and the subinertial energies are

$$\left. \begin{aligned} \hat{\overline{\text{KE}}} &= \frac{1}{8} \rho_0 U_0^2 \left( \frac{\omega^2 + f^2}{\omega^2} \right) \sum_{n=1}^{\infty} PP_n^2, \\ \hat{\overline{\text{APE}}} &= \frac{1}{8} \rho_0 U_0^2 \left( \frac{f^2 - \omega^2}{\omega^2} \right) \sum_{n=1}^{\infty} PP_n^2. \end{aligned} \right\} \quad (2.32)$$

Figure 3 illustrates the strong influence of rotation on the ridge-top energies for a 24 h tide with a fixed tidal amplitude  $U = 0.006 \text{ m s}^{-1}$ , a stratification of  $N = 0.0017 \text{ rad s}^{-1}$  (1 cph), in a depth of 1000 m for a ridge of height 500 m. Below the turning latitude, the total energy density at the ridge has a fixed value of  $2 \times$  that of the barotropic tide for this particular choice of parameters. At  $f_0^\circ$  this corresponds to a wavelike response with equipartitioned kinetic and potential energy. At higher latitudes the waves have a reduced potential energy, but an increased kinetic energy due to the along-ridge component whose speed increases with latitude as  $f/\omega$ . Above the turning latitude the response is evanescent, but the along-ridge oscillatory currents continue to grow with latitude. In contrast to superinertial behaviour, the available

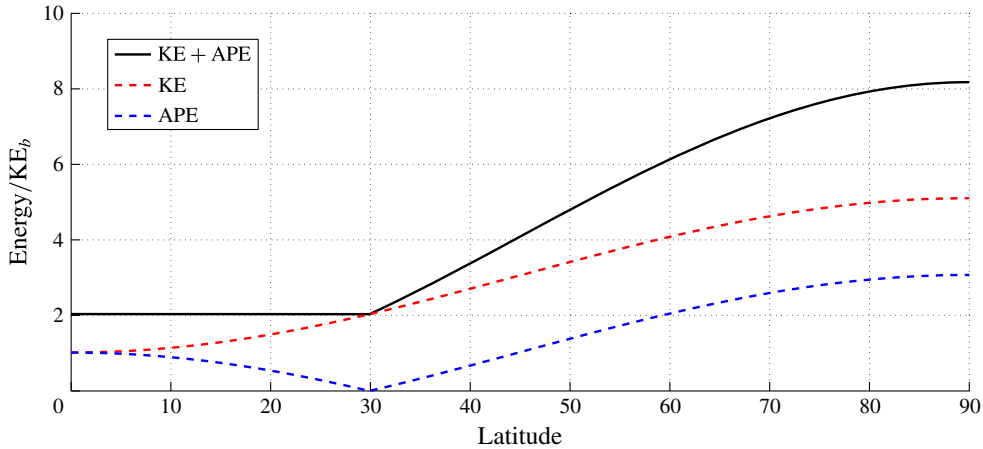


FIGURE 3. Depth- and time-averaged kinetic and available potential energies at  $x=0$  as a function of latitude, from theory.

potential energy of the evanescent response also grows with latitude as isopycnal displacements in the near field become large. The result is that for a fixed-amplitude barotropic tide, the ridge-crest energy density of the response increases with latitude once the flow is subinertial.

The increase in energy density with latitude also holds if the near-ridge, rather than ridge-crest, response is considered. Defining ‘near-ridge’ as within a distance of  $k^{-1}$  from the crest, and using the dispersion relations in (2.16), we see that lengthscale of the response decreases linearly in  $f$ . However, the ridge-top energy increases as  $f^2$ , causing the total near-ridge energy of the response to increase with latitude.

Despite the elevated near-topographic energy densities above the turning latitude, in this inviscid, two-dimensional analytical model there is no conversion of energy from the barotropic tide to the baroclinic response once the latitude is subinertial. In the absence of dissipation, conversion may only arise by the generation of radiating waves, whose phase-averaged energy flux is defined:

$$J = \frac{1}{T} \int_0^T \int_0^h \mathbf{u}p \, dz \, dt. \quad (2.33)$$

In the subinertial solution, pressure and cross-ridge velocity have a quadrature phase relation in time and as a result there is no outward radiating flux, in contrast to the superinertial solution where the pressure and cross-ridge velocity are in phase. However, in the subinertial solution pressure and along-ridge velocity are in phase, suggesting the potential for along-ridge radiation in a three-dimensional solution.

### 3. Numerical simulations

#### 3.1. Set-up

To test the above theory and explicitly illustrate the effects of changing latitude on tidal flows over topography, we use the MITgcm (Marshall *et al.* 1997) and solve the full nonlinear, non-hydrostatic equations for two-dimensional tidal flow over a steep Gaussian seamount on an  $f$ -plane. For all runs we set the tidal period to be 24 h,

and the Gaussian topography to have a height of 500 m in 1000 m of water, and a horizontal e-folding scale of 1000 m. Stratification is constant in depth with a Brunt–Väisälä period of 1 h ( $N = 0.0017 \text{ rad s}^{-1}$ ).

For the finite width bathymetry in these simulations, a measure of the linearity of the flow is given by a non-dimensional excursion length

$$\varepsilon_{rdg} = \frac{U_c}{\omega l_{rdg}}, \quad (3.1)$$

which compares the horizontal displacement of a fluid parcel each tidal cycle ( $l_{exc} = U_c/\omega$ ) to a characteristic width of the ridge ( $l_{rdg}$ ). Here  $U_c$  is the depth mean speed at the crest of the topography. Simulations are divided into two categories: the small excursion length simulations have a very small-amplitude barotropic tide ( $U_0 = 0.006 \text{ m s}^{-1}$ ), and the long excursion length simulations have a larger-amplitude tide ( $U_0 = 0.02 \text{ m s}^{-1}$ ). Generating tidal excursion lengths at the ridge crest of 160 and 550 m, respectively. An appropriate characteristic ridge width is determined at a depth from the crest determined by the vertical length scale associated with the flow:  $\delta = U_c/N$  (Winters & Armi 2013). For these parameters, we estimate the characteristic ridge widths to be 240 and 430 m, respectively. As such, the small excursion length simulations have  $\varepsilon_{rdg} < 1$ , and the large excursion length simulations have  $\varepsilon_{rdg} > 1$ .

A second important parameter is the topographic Froude number, which is defined as

$$Fr = \frac{U_0}{Nz_0}. \quad (3.2)$$

All simulations presented in this study have very small values of  $Fr$ , which in the ocean corresponds to tall topography where most of the tidal flow is unable to surmount the crest during all phases of the tide. Much of the tidal transport above the crest is accommodated in a relatively fast, thin, bottom intensified layer (Winters & Armi 2013).

In these simulations the topography is supercritical at all latitudes where the tide is superinertial, meaning that it is steeper than the characteristics of the fundamental frequency internal wave response. The barotropic tide is approximated in the model by the addition of a spatially uniform body force ( $G_u, G_v$ ) to each of the horizontal momentum equations such that in the absence of topography the flow is rectilinear in the  $x$ -direction and oscillatory with frequency  $\omega$  and amplitude  $U_0$  (Di Lorenzo, Young & Llewellyn Smith 2006). Specifically, we set

$$(G_u, G_v) = (-U_0\omega \sin(\omega t), U_0f \cos(\omega t)). \quad (3.3)$$

In the real ocean, the barotropic tide itself may be subject to dynamics including subinertial trapping (Longuet-Higgins 1968), however, its lengthscales are typically determined by the barotropic Rossby radius, of order 1000 km. As these scales are much larger than those being considered here, our spatially uniform approximation of the tide in these simulations is justified. The inclusion of a more realistic background tidal ellipse does not change the dynamics of these two-dimensional simulations, but it imposes greater computational demand by restricting the time step. Eleven small excursion length simulations are presented with  $f$  corresponding to latitudes,  $\theta = [0, 10, 20, 25, 35, 40, 50, 60, 70, 80, 90]^\circ$ . We use subscript notation to refer to each simulation, where, for example,  $f_{50^\circ}$  indicates the simulation was performed at a latitude of  $50^\circ$ . Two large excursion length simulations are performed at  $3.85^\circ$

and  $44.7^\circ$ . These latitudes are chosen because the theory of §2 predicts that the amplitude of near-crest isopycnal displacement, and therefore the available potential energy at the ridge crest, will be the same at each, even though the nature of the response will be fundamentally different. At  $\theta = 30^\circ$  we are very close to the turning latitude of a 24 h tide and the lengthscale,  $k^{-1}$ , is too large to fit in the computational domain, therefore we do not present results from this simulation.

We telescope our grids in the horizontal such that resolution is highest within 30 km of the ridge. Small excursion length simulations have an isotropic resolution of 15 m, and large excursion length simulations have an isotropic resolution of 5 m within this high-resolution region. In all cases, the domain has a total width of 300 km and is horizontally periodic. Baroclinic signals that reach the boundaries reenter the domain at the opposite boundary at a time determined by the phase speed of the signals and the width of the computational domain. We define an analysis region within  $\pm 4$  km of the ridge crest, and perform all analysis before these spurious signals reach the boundaries of our analysis domain, which occurs at a time easily identified using Hovmöller diagrams at fixed depth. For these simulations we have determined that between 120 and 144 h, five periods after the simulation starts, flows in the analysis region are uncontaminated by these reentrant waves.

As a check on the convergence of our numerical solutions, two of the small excursion length simulations ( $f_{10^\circ}$  and  $f_{50^\circ}$ ) are repeated with identical parameters but doubled resolutions to ensure that our solutions are not quantitatively resolution dependent. Evaluation of the kinetic energy budget in the double-resolution simulations reveal differences of less than 3% in the dominant terms, giving us confidence in the quantitative results of our standard-resolution simulations. We achieve good closure of the budget in the higher-resolution long excursion length simulations, where time mean residuals in the energy balance are approximately four times smaller than the smallest term in the kinetic energy budget (the dissipation rate). Closure of the budget in the small excursion length simulations have residuals that are comparable with computed dissipation rates, which themselves comprise around 1% of the largest terms in the budget. Residuals in this budget arise from spatial and temporal discretization errors in our post-simulation evaluation of the terms, in addition to numerical diffusion by the model numerical schemes.

The small excursion length simulations were performed with constant background viscosities of  $2 \times 10^{-3} \text{ m s}^{-2}$  corresponding to Reynolds numbers between 1500 and 5000, though the simulations are non-turbulent. The high-resolution long excursion length simulations additionally employ a Smagorinsky turbulence closure (Smagorinsky 1963), with a Smagorinsky coefficient of  $C_s^2 = 0.03$ . Diffusivities are  $8 \times 10^{-4} \text{ m s}^{-2}$  for all simulations, and no-slip boundary conditions are enforced at the topography. To minimize numerical diffusion, a seventh-order monotonicity preserving scheme is used for tracer advection (Daru & Tenaud 2004). Momentum advection is by a centred second-order scheme.

### 3.2. Small excursion length simulations

#### 3.2.1. Flow snapshots

Widefield snapshots of cross-ridge flow at 120 h are presented in figure 4 for the simulations at latitudes of  $10^\circ$  and  $50^\circ$ . In this and all subsequent snapshot figures the spatially constant background tide,  $u_b$ , has been removed. Parameters are the same as used in the linear analytic solution presented in figure 2, enabling a direct comparison of linear theory with model output. In the  $f_{10^\circ}$  simulation, the forcing frequency is

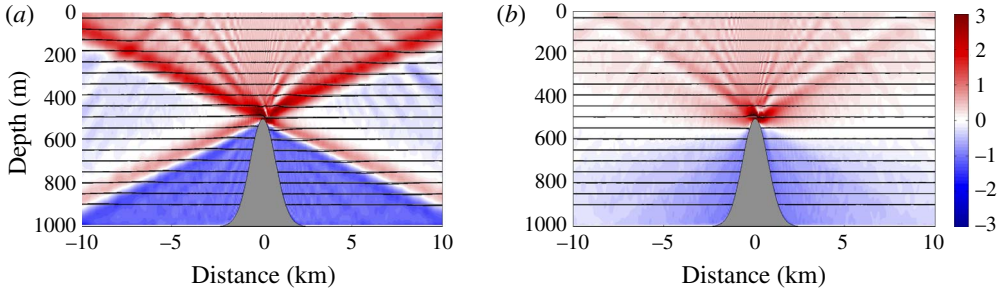


FIGURE 4. Widefield snapshots of  $u$ , with isopycnals contoured, for small excursion length simulation at (a)  $f_{10}$ , where the fundamental frequency response is radiating, and (b)  $f_{50}$ , where the fundamental frequency response is evanescent. Spatially constant background tide,  $u_b$ , has been removed. Non-dimensionalized by  $U_0$ .

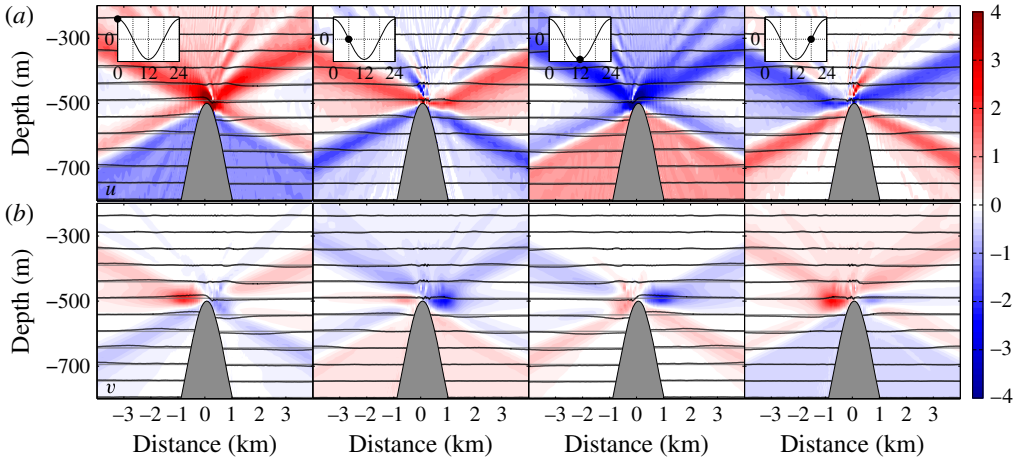


FIGURE 5. Snapshots of  $u$  (a) and  $v$  (b) with isopycnals (contoured) for small excursion length simulation at  $f_{10}$ , where the fundamental frequency response is radiating. Background tide,  $u_b$ , has been removed. Non-dimensionalized by  $U_0$ .

superinertial and the domain is filled with baroclinic energy associated with energetic radiating internal tides. Beams are present, formed from the superposition of linear internal wave modes. Their angles are dependent upon wave frequency according to the internal wave dispersion relation. Harmonics of the forcing frequency are visible at steeper angles, arising due to advection by the background tide (Bell 1975). In contrast, the subinertial  $f_{50^\circ}$  simulation has much less energy in the far field as energy at the forcing frequency is unable to radiate at this latitude. Beams at angles corresponding to harmonics of the fundamental frequency are present, indicating the generation of some radiating energy, however, their energy content is small.

Nearfield snapshots of the simulations at 6 h intervals between 120 and 138 h are shown in figures 5 and 6. Cross-ridge velocity,  $u$ , is presented in the upper panel, and along-ridge velocity,  $v$ , in the lower panel. Consistent with the linear solution, velocities in the along-ridge direction have an amplitude of  $fU_0/\omega$  and are therefore much smaller at  $10^\circ$  (figure 5) than at  $50^\circ$  (figure 6). In the  $f_{50^\circ}$  simulation, the quadrature phase relation between displacement and cross-ridge velocity is evident as

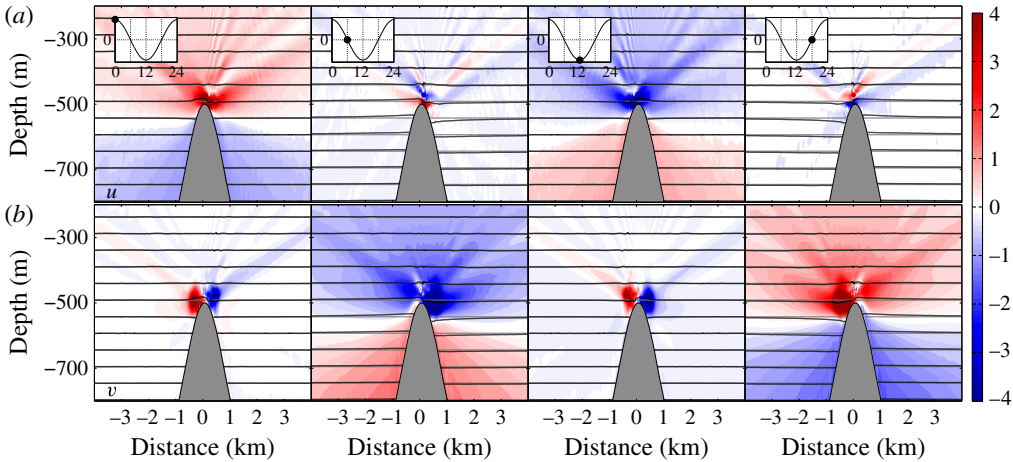


FIGURE 6. Snapshots of  $u$  (a) and  $v$  (b) with isopycnals (contoured) for small excursion length simulation at  $f_{50}$ , where the fundamental frequency response is evanescent. Background tide,  $u_b$ , has been removed. Non-dimensionalized by  $U_0$ .

isopycnal displacements occur with a 6 h lag behind cross-ridge flows. In agreement with the theory of § 2, both along- and cross-ridge velocities are baroclinic away from topography. The periodic nature of the symmetric tidal flow is demonstrated as the third and fourth panels are mirror images of the first and second panels, with the colors reversed. Time mean along-ridge jets form along the flanks of the ridge and are most clearly visible at 0 and 12 h of the snapshots, and are discussed in detail in the next section.

### 3.2.2. Phase-averaged flows

Despite the small amplitudes of the tide in these simulations, nonlinear effects generate significant rectified along-ridge flows near the crest of the ridge whose magnitude increases with latitude. In the deep ocean, tidally rectified flows arise under the combined influence of a Stokes drift associated with the Coriolis turning of a fluid parcel as it changes its water depth, and an Eulerian mean current (Huthnance 1973; Loder 1980). In the shallow water near the ridge crest, continuity and Coriolis turning cause the tidal ellipse to be larger than in deeper water. The tidal Stokes drift arises as fluid parcels advected between deep and shallow water each tidal cycle experience asymmetric along-ridge flows, leading to a time-mean drift along the ridge (in the northern hemisphere the drift is with shallow water to the left). However, in the shallow water close to the crest fluid parcels experience greater friction than in deeper water, and an Eulerian mean flow is established such that, combined with the Stokes drift, fluid parcels experience no time mean accelerations or drag over each tidal cycle. The Eulerian mean flow is in the opposite sense to the Stokes drift such that along-ridge parcel velocity is enhanced in low friction (deeper) regions relative to high friction (shallower) regions, and the net drag is zero. The resulting mean Lagrangian current is in the same sense as the Eulerian current (shallow water to the right, in the northern hemisphere), but is smaller due to the influence of the mean Stokes velocity. The generation of these flows has been studied for a stratified fluid over small-amplitude topography in some detail (Maas & Zimmerman (1989a) and

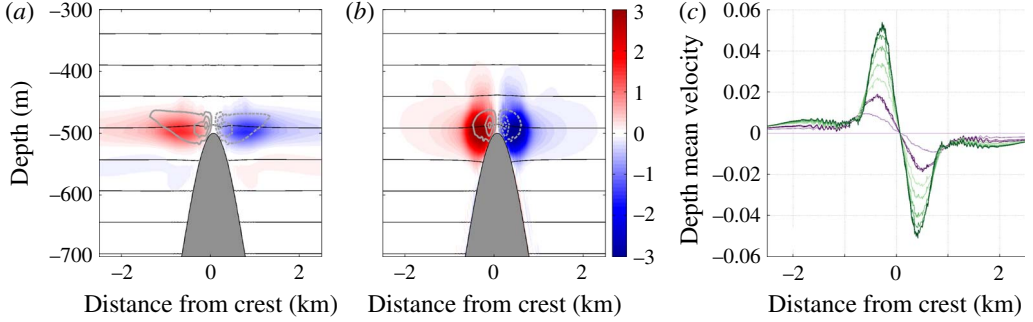


FIGURE 7. Eulerian mean along-ridge velocities normalized by  $U_0$  at (a)  $f_{10^\circ}$  and (b)  $f_{50^\circ}$ . Grey contours are  $x$ - $z$  streamfunction. (c) Depth mean along-ridge velocities from all small excursion length simulations. Higher latitudes are darker, with purples indicating superinertial latitudes and greens indicating subinertial latitudes.

Maas & Zimmerman (1989b), hereafter MZ88a and MZ88b, respectively). MZ88b find that stratification causes the rectified flows to be bottom trapped, and associated with Eulerian mean cross-isobath circulations. In this section we illustrate these flows in our simulations from both the Eulerian and Lagrangian reference frame and find good qualitative agreement between the small-amplitude topography theory presented in MZ88b, and the rectified flows occurring in these finite-amplitude topography simulations.

Eulerian time-mean along-ridge currents (colour),  $x$ - $z$  streamfunction (grey contours) and isopycnal displacements (black contours) from the analysis period for the simulations at  $f_{10^\circ}$  and  $f_{50^\circ}$  are shown in figure 7(a,b). The Eulerian mean streamfunction is computed by integrating the time mean cross-ridge component in  $z$ , with the integration constant set to ensure continuity over the ridge. In all simulations with  $f \neq 0$ , a mean flow develops that is predominantly composed of a pair of along-ridge jets with anticyclonic vertical vorticity at the ridge crest, with a general trend that the jets become faster as latitude increases (figure 7c). Peak jet speeds in the  $f_{50^\circ}$  simulation are in excess of  $3U_0$  and are located at around the depth of the crest of the topography (note that at this latitude the oscillatory along-ridge response has a magnitude of  $fU_0/\omega = 1.5U_0$ ). As predicted in MZ88b, these Eulerian time-means exhibit secondary circulations in the  $x$ - $z$  plane: jet-centred cells with peak downwards velocities of around  $0.25U_0$  at the crest, and weaker upward velocities near the outside of each of the jets. The phase mean along-ridge jets in the  $f_{10^\circ}$  simulation are weaker and extend further in the horizontal.

We compute the Eulerian mean momentum balance by performing a Reynolds decomposition of the fields such that they are composed of three parts: an Eulerian phase-averaged component (angle brackets), the oscillatory baroclinic response component (primes), and, in the case of the cross-ridge velocity, the spatially uniform background tide ( $u_b$ ):

$$\left. \begin{aligned} u &= \langle u \rangle + u' + u_b; & v &= \langle v \rangle + v'; & w &= \langle w \rangle + w', \\ p &= \langle p \rangle + p'; & b &= \langle b \rangle + b'. \end{aligned} \right\} \quad (3.4)$$

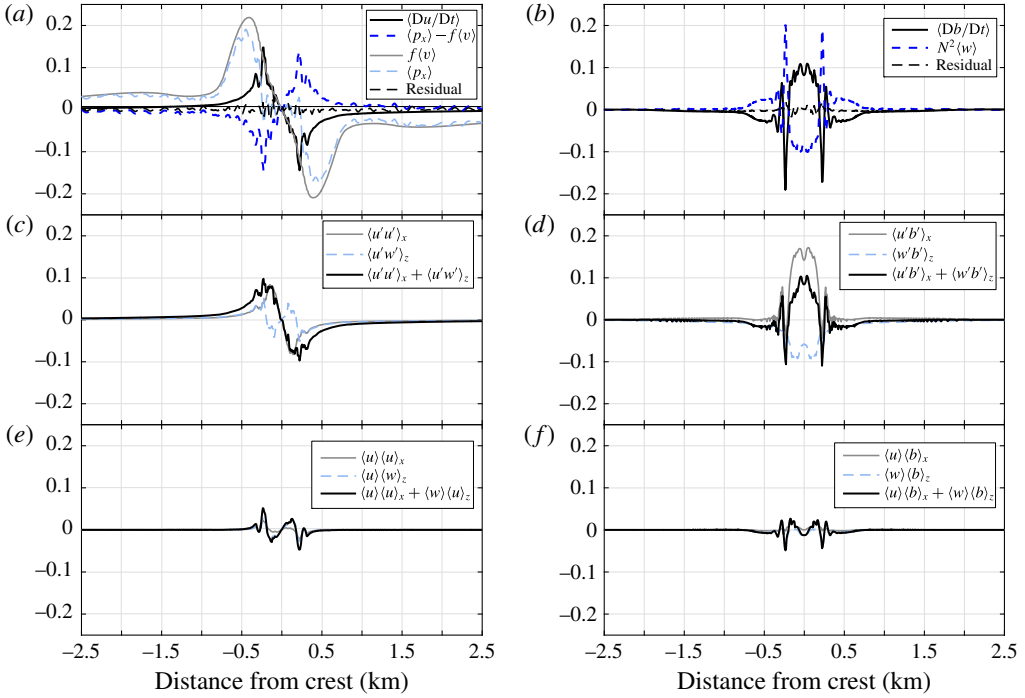


FIGURE 8. Depth mean near-ridge (*a,c,e*) *x*-momentum budget (non-dimensionalized by  $fU_0$ ) and (*b,d,f*) buoyancy budget (non-dimensionalized by  $w_0N^2$ ) for  $f_{50^\circ}$ . Thick lines in upper panels indicate the dominant balance in the equations. Lower panels break down the advective terms into perturbations and means.

These expressions are substituted into the nonlinear equations of motion, and averaged over one tidal period:

$$\left. \begin{aligned}
 \langle u \rangle_t + \langle p \rangle_x - f \langle v \rangle - \nu \nabla^2 \langle u \rangle &= -(\langle u_b u' \rangle_x + \langle u' u' \rangle_x + \langle w' u' \rangle_z + \langle u \rangle \langle u \rangle_x + \langle w \rangle \langle u \rangle_z), \\
 \langle v \rangle_t + f \langle u \rangle - \nu \nabla^2 \langle v \rangle &= -(\langle u_b v' \rangle_x + \langle u' v' \rangle_x + \langle w' v' \rangle_z + \langle u \rangle \langle v \rangle_x + \langle w \rangle \langle v \rangle_z), \\
 \langle w \rangle_t + \langle p \rangle_z - \langle b \rangle - \nu \nabla^2 \langle w \rangle &= -(\langle u_b w' \rangle_x + \langle u' w' \rangle_x + \langle w' w' \rangle_z + \langle u \rangle \langle w \rangle_x + \langle w \rangle \langle w \rangle_z), \\
 \langle b \rangle_t + N^2 \langle w \rangle - \kappa \nabla^2 \langle b \rangle &= -(\langle u_b b' \rangle_x + \langle u' b' \rangle_x + \langle w' b' \rangle_z + \langle u \rangle \langle b \rangle_x + \langle w \rangle \langle b \rangle_z), \\
 \langle u \rangle_x + \langle w \rangle_z &= 0.
 \end{aligned} \right\} \quad (3.5)$$

The advective terms are grouped on the right-hand side of the equations, and represent forcing terms for the Eulerian mean fields. Three types of nonlinear interaction can give rise to a momentum flux into the Eulerian mean: (1) self-interaction of the primed fields (Reynolds stresses); (2) self-interaction of the mean fields; and (3) interaction of the barotropic tide with the primed fields. Terms making up the momentum and buoyancy budgets were computed at the beginning of the fifth period for the double-resolution simulation at  $f_{50^\circ}$  in a region close to the crest of the ridge. The across-ridge momentum and buoyancy budgets and are shown in figure 8, where (*a,b*) shows the dominant terms and budget residual. All of the nonlinear terms are included in  $\langle Du/Dt \rangle$  and  $\langle Db/Dt \rangle$ , respectively.

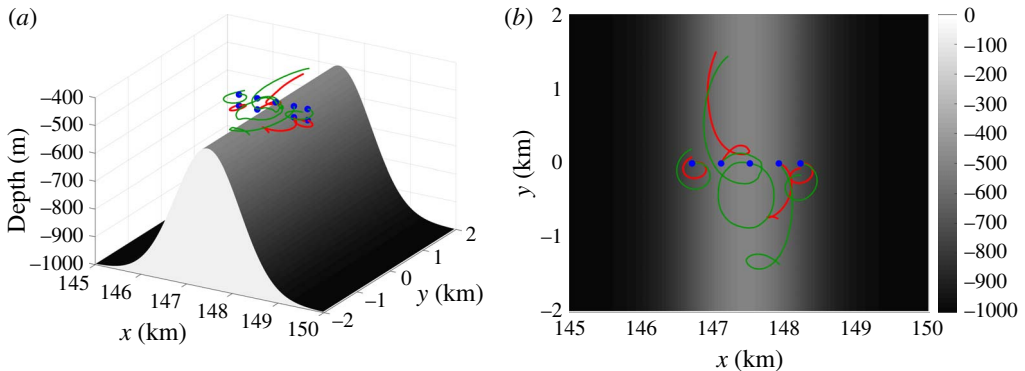


FIGURE 9. Particle trajectories over one period for 9 particles seeded at 120 h in  $f_{50}$  simulation: (a) side view; (b) plan view. Green tracks are for particles seeded at  $-480$  m, red tracks are particles seeded at  $-520$  m. Blue dots indicate starting positions.

Consistent with the expected balance for tidally rectified flows (e.g. Loder 1980), the across-ridge ( $x$ ) momentum balance for the Eulerian mean flow is predominantly in geostrophic balance (figure 8*a*, pale blue dashed and grey solid lines), with a residual supported by nonlinear terms. The terms corresponding to the rate of change of the mean cross-ridge flow and viscous diffusion of mean  $x$ -momentum were found to be negligibly small compared with the other terms and are not explicitly shown (the time dependent terms make a small contribution to  $\langle Du/Dt \rangle$  and  $\langle Db/Dt \rangle$ ). The nonlinear terms are broken down in figure 8(*c-f*), and show that the dominant terms are the Reynolds stresses, shown in figure 8(*c*).

Terms in the Eulerian buoyancy budget are shown in figure 8(*b*). Figure 8(*a,b*) illustrates the balance between nonlinear terms and the Eulerian vertical velocity. Once again, the time derivative and diabatic terms are small compared with the others and are not shown. The smallness of the diffusive term confirms that despite the relatively large Eulerian vertical velocities, fluid parcels do not cross isopycnals in the time mean, underscoring the importance of a Lagrangian frame of reference when considering time mean fluid motion in oscillatory flows. Eulerian mean vertical velocities are mainly supported by Reynolds stresses (figure 8*d*), and to a lesser extent by interactions of the Eulerian mean fields (figure 8*f*).

Whilst the diabatic and unsteady terms are negligibly small in the across-ridge momentum and buoyancy budgets, they are small but non-zero in the along-ridge ( $y$ ) momentum balance (not shown), indicating that the jets are slowly accelerating at the time that the budget was diagnosed. Mixing results in a volume of intermediate density fluid close to the crest of the ridge that slowly increases over the course of the simulation (see § 3.3). Chen & Beardsley (1995) found similar processes to be occurring in their simulations of stratified tidal flow over a shallow two-dimensional ridge where it generated a tidal mixing front, which, through Rossby adjustment, became associated with a frontal jet. The generation of mixed fluid in our simulations provides a small but steadily increasing contribution to the rectified flows generated by Coriolis turning and friction.

Individual particle trajectories were computed over one period for the flow as a post-processing step by integrating the 10 min output fields using a Runge–Kutta fourth-order scheme. Paths are dependent on the phase of the tide at which the particles were seeded, and figure 9 shows nine paths initiated at slack tide before eastward flow in

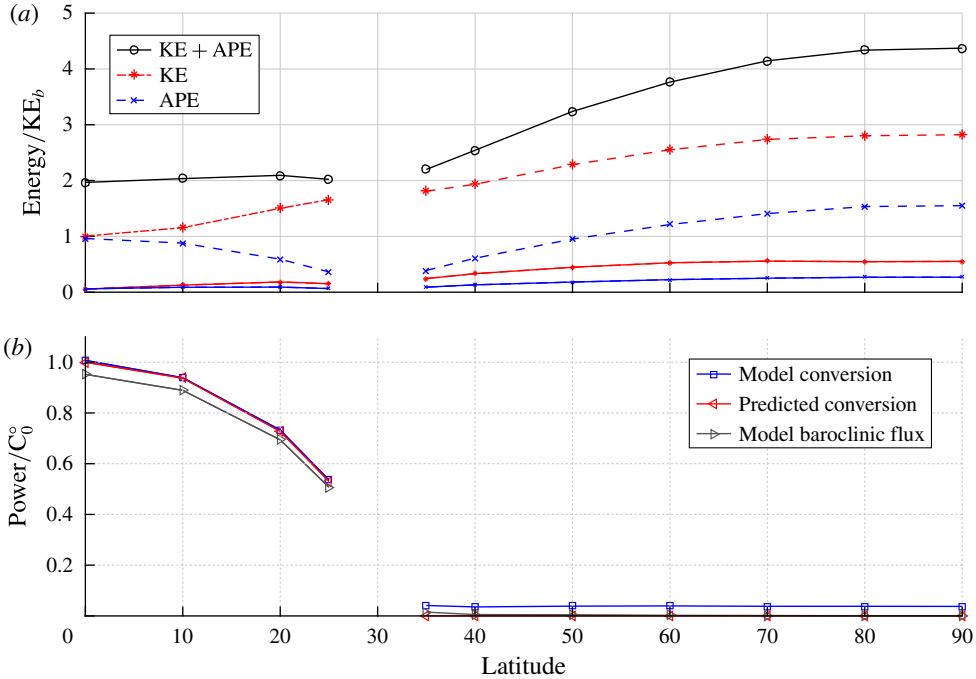


FIGURE 10. Energies averaged over 2 km region at ridge crest. (a) Thick lines: phase mean kinetic (red dashed), available potential (blue dashed) and total energy (black solid). Thin lines: kinetic (red) and available potential (blue) energy in the time mean flow. (b) Barotropic–baroclinic conversion from theory (red) and model (blue), and baroclinic flux out of region (grey).

the  $f_{50^\circ}$  simulation. Particles close to the crest exhibit looping trajectories along the ridge, as they move under the combined influence of Stokes drift and the Eulerian mean flow, spending less time in shallower water (higher friction) than in deeper water (lower friction) such that they experience no net drag. Short-wavelength oscillations are apparent in some tracks as particles pass through nonlinear lee waves. Further away from the crest, particles exhibit tracks that are much more elliptical, and close to those expected from the zero-order linear solution. Particle tracks in the  $f_{10^\circ}$  simulation (not shown) are qualitatively similar, but have smaller displacements along the ridge crest due to weaker rectified flows.

### 3.2.3. Energetics

Tidal averages of kinetic and available potential energies in the region above the topography are shown in figure 10(a). The finite width of the model ridge makes a precise comparison with theory impossible, as such we present the spatial average in a region 2 km wide and centred at the crest of the ridge. For comparison with the theoretical results shown in figure 3, the kinetic energy is computed from only the velocity field arising from the presence of the topography, i.e. with the time-dependent but spatially constant background tide,  $u_b$ , removed.

Consistent with theory, average ridge-crest energy is approximately constant below the turning latitude, but increases with latitude where the barotropic tide is subinertial. Where the tide is superinertial, the radiated wave field has a spatially constant energy

density, and integrals over the analysis region compare well with the energy densities predicted by theory. However, when the tide is subinertial the response is spatially varying, and decays exponentially away from topography. In this case the influence of the finite width of the topography on the spatial average causes the measured energy density to be much smaller than that predicted for the knife-edge ridge.

Kinetic and potential energies associated with the Eulerian time mean flow are shown in thin lines in figure 10(a). Even though the phase-averaged flows have velocities comparable with the tidal amplitude, they constitute much less energy than their time-dependent counterparts due to their limited spatial extent. The amplitudes of these mean flows tends to increase with latitude up to  $70^\circ$  and is roughly constant above that (figure 7).

Terms in the baroclinic energy budget are evaluated following (Kang & Fringer 2012) for the analysis region, and are shown in figure 10(b). The predicted rate of conversion of barotropic to baroclinic energy by a knife edge ridge with the same parameters (stratification, tidal amplitude and height) are also shown, and the conversion predicted at  $\theta = 0$  is used to non-dimensionalize all values (Llewellyn Smith & Young 2003). Modelled conversion is remarkably well predicted by the knife-edge model, despite the nonlinearities and finite width of the numerical simulation. Conversion decreases with latitude up to the turning latitude, and is negligible beyond, as the evanescent response does not extract energy from the barotropic tide in steady state. At superinertial latitudes, model baroclinic fluxes are comparable with conversion as most of the converted energy radiates out of the domain in the form of internal tides. Differences between the conversion and baroclinic flux arises from the dissipation of baroclinic energy within the domain. When the tide is subinertial, radiated fluxes are negligible, and all converted barotropic to baroclinic energy is dissipated locally.

### 3.3. Long excursion length simulations

Nearfield mixing can arise through both breaking tidal lee waves and transient hydraulic jumps (Musgrave *et al.* 2016), influencing the overall tide-topography energy budget by dissipating energy in the nearfield, and reducing the radiated internal wave flux (Klymak, Legg & Pinkel 2010; Rapaka, Gayen & Sarkar 2013). In this section we present the results of two simulations having relatively long excursion lengths ( $l_{exc} \approx l_{rdg}$ ), and contrast the development of nearfield mixing when the tide is subinertial, then superinertial. The tidal amplitudes of these flows are  $0.02 \text{ m s}^{-1}$ , which is small, even in the deep ocean. Though the cross-ridge kinetic energy of the response is the same at all latitudes, the along-ridge kinetic energy and available potential energy depends on latitude. These simulations were performed at latitudes of  $3.85^\circ$  and  $44.7^\circ$ , where theory predicts that the amplitude of the ridge-top buoyancy anomaly (potential energy) will be the same, enabling as close to an equivalent comparison as possible.

Snapshots of the flow at 6 h intervals during the fifth period of the simulation are shown in figures 11 (superinertial) and 12 (subinertial). As in the small excursion length simulations, the superinertial tide generates radiating energy at the fundamental frequency and its harmonics which forms beams at characteristic slopes emanating from the topographic crest. Close to the crest, the wavefield constructively superposes during peak cross-ridge flow to form tidal lee waves: time-dependent beam-like features that have slopes that change with the tide as the composite frequencies disperse (Bell 1975; Musgrave *et al.* 2016). The subinertial simulation has some

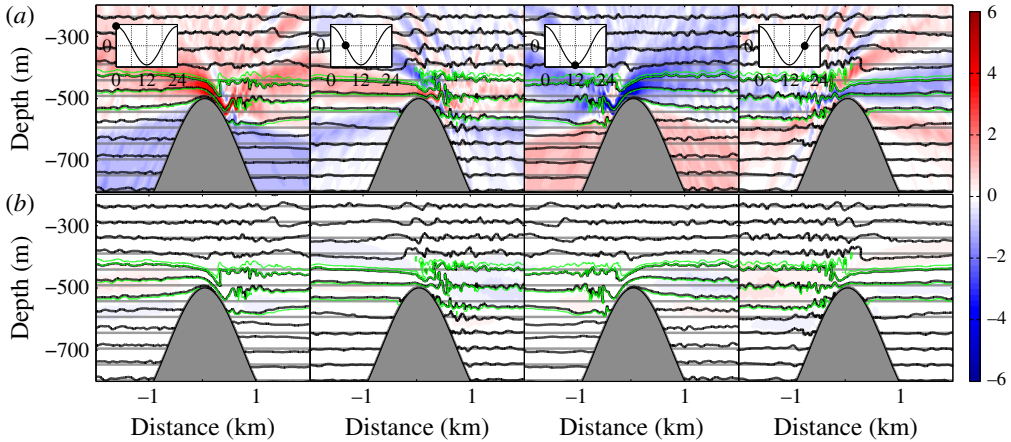


FIGURE 11. Snapshots of cross-ridge velocity  $u$  (a) and along-ridge velocity  $v$  (b) with isopycnals (contoured) for nonlinear simulation ( $U_0 = 0.02 \text{ m s}^{-1}$ ) at  $f = 3.85^\circ$ , where the fundamental frequency response is radiating. Green contours indicate temperature classes which have increased in volume through mixing.

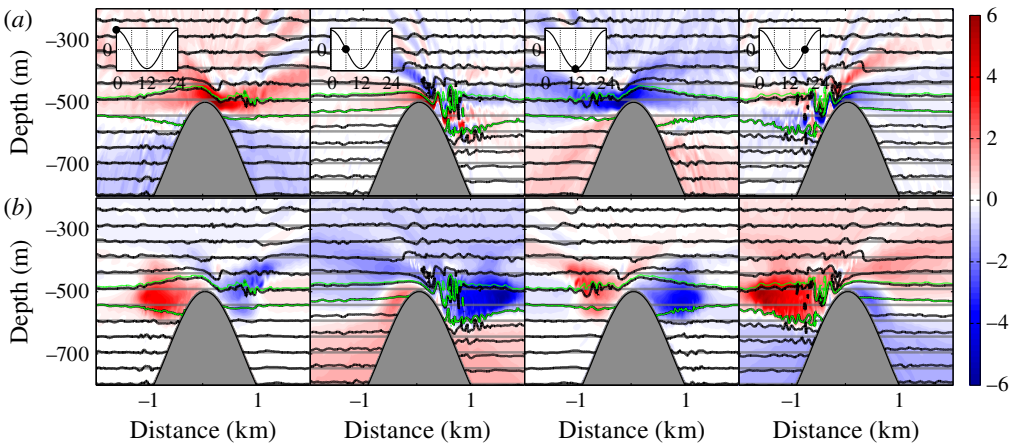


FIGURE 12. Snapshots of cross-ridge velocity  $u$  (a) and along-ridge velocity  $v$  (b) with isopycnals (contoured) for nonlinear simulation ( $U_0 = 0.02 \text{ m s}^{-1}$ ) at  $f = 44.7^\circ$ , where the fundamental frequency response is evanescent. Green contours indicate temperature classes which have increased in volume through mixing.

energy at harmonics, but the response at the fundamental frequency is trapped and associated with large-amplitude along-ridge flows. The quadrature phase relation between ridge-top flow and isopycnals is more obvious in these large-amplitude simulations, with the subinertial simulation having large isopycnal displacements during slack tide (hours 6 and 18). In hours 0 and 12, isopycnals very close to the crest of the ridge on its upstream side exhibit vertical displacements that are not predicted by the linear theory in § 2, and are associated with the phase-averaged jets.

Area integrated dissipation rates within  $\pm 4 \text{ km}$  of the ridge crest are presented for each simulation during the fifth period in figure 13(a). In these two-dimensional

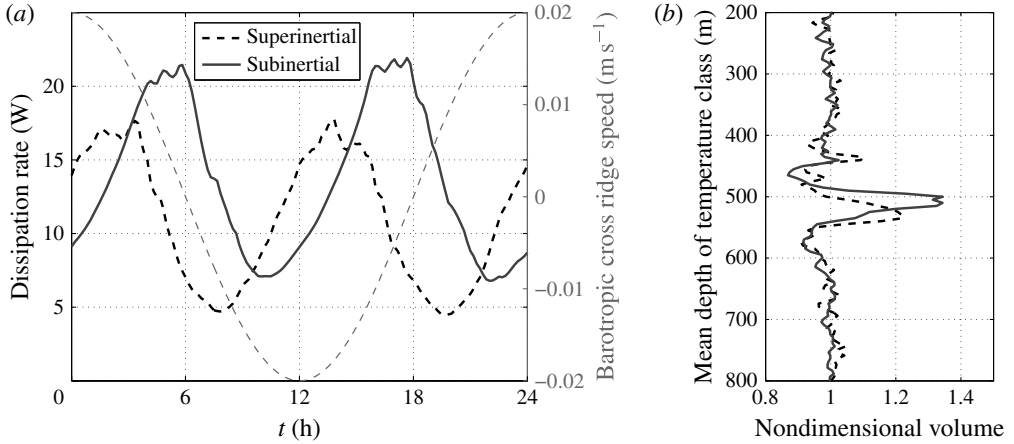


FIGURE 13. (a) Integrated dissipation rate within  $\pm 4$  km of the crest versus time during the fifth period. Thin dashed line is background tide,  $u_b$ . (b) Volume of fluid occupied by given temperature class at 120 h, non-dimensionalized by volume occupied at 0 h.

simulations, computed dissipation rates are not representative of dissipation associated with fully turbulent, three-dimensional flows at high Reynolds number. Nevertheless, their relative values and timings provide insight on which of the two simulations are more dissipative, and when during the tidal cycle the dissipation occurs. Dissipation rates take larger values and peak later in the tidal cycle for the subinertial simulation compared with the superinertial simulation. In the superinertial simulation tidal transport is in phase with isopycnal displacement at the ridge crest, and peak dissipation lags peak tidal flow by around an eighth of a period as dissipative processes in the hydraulic jump continue to grow even once the cross-ridge tidal transport starts to decrease. In the subinertial simulation isopycnal displacement lags tidal transport by a quarter period at the ridge crest, and peak dissipation rates are both larger than in the superinertial simulation, and lag peak tidal flow by almost a quarter of a period, occurring significantly later in the tidal cycle than in the superinertial case. As the cross-ridge transport relaxes, the combination of upward-moving isopycnals on the upstream side, and downward moving isopycnals on the lee side causes the near-bottom, hydraulically controlled jet to persist for longer, with the hydraulic jump developing in a region of relatively low stratification (associated with large isopycnal displacement) and generating a more dissipative hydraulic jump than in the superinertial case. In the latter situation, the relaxing tidal transport is associated with increasing downstream stratification.

We assess the vertical distribution of mixing in each simulation within the analysis domain ( $\pm 4$  km of the ridge crest) by defining an evenly spaced set of temperature classes, then computing the volume of fluid occupied by each temperature class at the beginning of the simulation, and at 120 h of the simulation. Figure 13(b) shows the volume of fluid occupied by each temperature class, non-dimensionalized by its initial volume for both the sub- and superinertial simulations. Volumes different than one indicate that diabatic processes have mixed fluid into or out of that temperature class. Both simulations show distinct mixing peaks at depths of  $\sim 500$  m, corresponding to relatively weakly stratified fluid that develops close to the peak. Adjacent temperature classes occupy a reduced volume of fluid, indicating relatively

high stratifications surrounding the mixed fluid. The superinertial simulation has a second, smaller peak at around 430 m depth. The temperature classes which have grown (non-dimensional volumes greater than one) are outlined in green contours in figures 11 and 12. Musgrave *et al.* (2016) distinguish between mixing arising from hydraulic jump-like features which occur on the flanks of topography, and mixing arising from convective instability of the radiating lee wave component, which occurs at shallower depths, mainly above the ridge crest. The lack of a second, shallower peak in the subinertial simulation is consistent with the evanescent (non-radiating) fundamental frequency response, and consequently a much smaller radiating component than in the superinertial case. The dominant mixing mechanism here is a transient hydraulic jump of the bottom trapped cross-ridge jet, forming on the flanks of the ridge each tidal cycle. In the superinertial simulation, the constructive interference of the fundamental and harmonic responses is of large enough amplitude to generate breaking and mixing in a radiating tidal lee wave, forming a second, smaller peak in mixing above the top of the ridge. It is notable that the subinertial simulation is more dissipative, despite the relative contribution from the radiating component being much smaller in this case.

#### 4. Trapped internal tides in three dimensions

The distinctly different nature of the evanescent compared with the radiating response results in changes not only to the magnitude and spatial distribution of tidal energy near topography, but also the timing, structure and evolution of nearfield tidally driven mixing. In addition, nonlinear effects generate fast along-ridge time mean currents, even when tidal amplitudes are small. A natural question that arises is to what extent these idealized two-dimensional results apply in a more general three-dimensional setting, and whether additional phenomena may become important.

Our imposition of two-dimensional solutions excludes *a priori* features with along-ridge variation, including trapped topographic waves, which have been observed at several high-latitude locations (Padman *et al.* 1992; Kunze & Toole 1997). The structure of these trapped waves can be determined for specific topographies and stratifications by numerically solving an eigenvalue problem whose eigenmodes correspond to the resonant modes of the topography (Huthnance 1978; Brink 1989; Codiga 1997). Trapped modes have discrete subinertial frequencies, and propagate anticyclonically around bathymetry. When the eigenfrequencies of the trapped modes are close to that of a tidal constituent, trapped tides at that frequency may be resonantly excited, generating relatively large-amplitude tidal currents close to the topography (Chapman 1989). Unlike the two-dimensional forced solutions discussed in this paper, the eigenmodes corresponding to trapped tides are constructed such that they individually satisfy a boundary condition of no-flow through the boundary. Conversely, in the forced tidal problem, solutions are required to add to the background tide such that there is no flow through the boundary, which means that the solutions themselves have a component perpendicular to the boundary. Despite this distinction, we note that in the subinertial solution, the phase relation between displacement and along-ridge flow is consistent with propagation along the ridge (if along-ridge variation was allowed). As a result, the forced response described in this paper will resonantly excite the trapped eigenmodes of the topography if the topographic length scales and ambient stratification are such that the eigenfrequencies of the topography are close to the forcing frequency. For isolated topographies, the potential for such resonant forcing may have important consequences for nearfield mixing and dissipation, as a large-amplitude response is subject to nonlinearities and breaking.

Even in the absence of a resonance between the forced response and the eigenmodes of the topography, we expect that the characteristics of the subinertial forced solutions described here are relevant in three dimensions, generating strong along-ridge flows that are phase locked with the background tide and having displacements and velocities that increase, and off-ridge length scales that decrease at higher latitudes.

## 5. Discussion and conclusions

In this paper we have examined the two-dimensional response of a stratified ocean to subinertial tidal forcing, and contrasted it to the relatively well-studied response to superinertial tidal forcing. Analytic solutions for a tall, infinitely thin barrier predict a latitudinal increase in the energy density at the ridge-crest when the tide is subinertial, arising from large along-ridge flows and isopycnal displacements. This is confirmed in a series of numerical simulations, which additionally illustrate the distinctive evanescent nature of the response. The elevated energy density of near-ridge subinertial tidal flows may strongly influence regional mixing at high latitudes, affecting critical climate processes including ice melt and ocean–atmosphere heat exchange.

All simulations with  $f \neq 0$  generate along-ridge rectified currents, demonstrating the importance of nonlinearity in these flows despite the small barotropic amplitudes. The speed of the Eulerian mean currents increase with latitude, with peak speeds reaching  $4u_0$  at latitudes of  $80^\circ$ , though the jet speeds continue to increase during our simulations. The time mean flows are primarily associated with the Coriolis mechanism described by Huthnance (1973), whereby Coriolis turning and frictional drag cause fluid parcels to acquire relative vorticity. Additional routes for nearfield dissipation may be associated with these currents in three dimensions, either by interaction with along-bathymetric features which could lead to along-ridge hydraulic processes, or even via the generation of Kelvin–Helmholtz-type instabilities. Using the Eulerian mean field at  $f_{50^\circ}$ , and with  $N = 1$  cph, we estimate a vertical shear of  $\sim 9 \times 10^{-4} \text{ s}^{-1}$ , which results in a Richardson number of around 3.7. However, the influence of nearfield mixing on locally reducing stratification, combined with time-dependent changes in shear and stratification has the potential to reduce the Richardson number during some phases of the tide such that instabilities in the along-ridge flow may play an important role. In addition, the Lagrangian transport associated with these jets may be important for high-latitude coastal processes, transporting and mixing water masses across the shelf-break and providing a pathway for the regional transport of tracers and biological material (Flexas *et al.* 2015).

A pair of simulations with larger-amplitude tides ( $0.02 \text{ m s}^{-1}$ ) at latitudes that are superinertial and subinertial for the 24 h tide show that the subinertial simulation is relatively more dissipative, with peak dissipation occurring around  $\pi/2$  after peak barotropic velocity in the subinertial case, compared to around  $\pi/4$  in the superinertial case. Enhanced mixing in the subinertial simulation is due to reduced stratification downstream of the crest when the transient hydraulic jump is developing. The vertical distribution of mixing in both simulations is similar, though the superinertial simulation has more mixing higher in the water column, associated with the radiating lee wave response. In both simulations, most of the mixing occurs on the near-crest flanks of the ridge, and is associated with hydraulic control of a bottom intensified cross-ridge jet.

The generation of evanescent wave responses is not restricted to subinertial frequencies. Maas (2011) shows that certain topographic shapes may be expected

to generate evanescent baroclinic signals at specific frequencies, even when the tidal forcing is superinertial. As such, the enhanced nearfield mixing that we observe in this study may have a broader relevance to superinertial evanescent responses.

The idealized nature of this study invites further, more realistic investigation. In particular, the influence of three-dimensional topography and a varying stratification are relevant in an oceanic context. Our restriction to constant stratification is applicable in the deep ocean, where a trapped response may not extend as far as a pycnocline. However, in shallow water this is not the case, and an understanding of how variations in stratification might affect the solution may be important. The effects of three-dimensional topography, and particularly the interaction of the forced response discussed here with three-dimensional trapped subinertial free modes may lead to significantly more nearfield dissipation and mixing compared with when the tide is superinertial. This additional complexity may indicate that parametrizing the dissipation of subinertial tidal constituents may prove more complicated than their superinertial counterparts.

### Acknowledgements

We thank N. Grisourd for helpful discussions relating to this work, and M. Nikurashin for help setting up the numerical model. Computing was performed on the Yellowstone Supercomputer, NSF award number ANT-0961218. R.C.M. acknowledges funding from the Office of Naval Research under grant ONR N00014-12-1-0943 and from the National Science Foundation under grant NSF OCE 1129763. M.M. acknowledges the National Science Foundation (NSF) for support of this research through grants OCE-1234473 and PLR-1425989.

### REFERENCES

- BAINES, P. G. 1982 On internal tide generation models. *Deep-Sea Res. A* **29** (3), 307–338.
- BELL, T. H. 1975 Lee waves in stratified flows with simple harmonic time dependence. *J. Fluid Mech.* **67** (4), 705–722.
- BRINK, K. H. 1989 The effect of stratification on seamount-trapped waves. *Deep-Sea Res. A* **36** (6), 825–844.
- BRINK, K. H. 1990 On the generation of seamount-trapped waves. *Deep-Sea Res. A* **37** (10), 1569–1582.
- BRINK, K. H. 2011 Topographic rectification in a stratified ocean. *J. Mar. Res.* **69**, 483–499.
- CHAPMAN, D. C. 1989 Enhanced subinertial diurnal tides over isolated topographic features. *Deep-Sea Res. A* **36** (6), 815–824.
- CHEN, C. & BEARDSLEY, R. C. 1995 A numerical study of stratified tidal rectification over finite-amplitude banks. Part 1: symmetric banks. *J. Phys. Oceanogr.* **25**, 2090–2110.
- CODIGA, D. L. 1997 Physics and observational signatures of free, forced, and frictional stratified seamount-trapped waves. *J. Geophys. Res.* **102** (C10), 23009–23024.
- DARU, V. & TENAUD, C. 2004 High order one-step monotonicity-preserving schemes for unsteady compressible flow calculations. *J. Comput. Phys.* **193** (2), 563–594.
- DI LORENZO, E., YOUNG, W. R. & LLEWELLYN SMITH, S. G. 2006 Numerical and analytical estimates of M<sub>2</sub> tidal conversion at steep oceanic ridges. *J. Phys. Oceanogr.* **36** (6), 1072–1084.
- EGBERT, G. D. & RAY, R. D. 2003 Semi-diurnal and diurnal tidal dissipation from TOPEX/Poseidon altimetry. *Geophys. Res. Lett.* **30** (17), doi:[10.1029/2003GL017676](https://doi.org/10.1029/2003GL017676).
- FLEXAS, M. M., SCHODLOK, M. P., PADMAN, L., MENEMENLIS, D. & ORSI, A. H. 2015 Role of tides on the formation of the Antarctic slope Front at the Weddell–Scotia confluence. *J. Geophys. Res. Oceans* **120**, 3658–3680.

- GERKEMA, T. & SHRIRA, V. I. 2005 Near-inertial waves in the ocean: beyond the 'traditional approximation'. *J. Fluid Mech.* **529**, 195–219.
- GREEN, J. A. M. & NYCANDER, J. 2013 A comparison of tidal conversion parameterizations for tidal models. *J. Phys. Oceanogr.* **43** (1), 104–119.
- HASUMI, H. & SUGINOHARA, N. 1999 Effects of locally enhanced vertical diffusivity over rough bathymetry on the world ocean circulation. *J. Geophys. Res.* **104** (C10), 23367–23374.
- HUTHNANCE, J. M. 1973 Tidal current asymmetries over the Norfolk Sandbanks. *Estuar. Coast. Mar. Sci.* **1**, 89–99.
- HUTHNANCE, J. M. 1978 On coastal trapped waves: analysis and numerical calculation by inverse iteration. *J. Phys. Oceanogr.* **8** (1), 74–92.
- JAYNE, S. R. 2009 The impact of abyssal mixing parameterizations in an ocean general circulation model. *J. Phys. Oceanogr.* **39** (7), 1756–1775.
- KANG, D. & FRINGER, O. B. 2012 Energetics of barotropic and baroclinic tides in the Monterey Bay area. *J. Phys. Oceanogr.* **42** (2), 272–290.
- KLYMAK, J., LEGG, S. & PINKEL, R. 2010 A simple parameterization of turbulent tidal mixing near supercritical topography. *J. Phys. Oceanogr.* **40**, 2059–2074.
- KUNZE, E. & TOOLE, J. M. 1997 Tidally driven vorticity, diurnal shear, and turbulence atop Fieberling Seamount. *J. Phys. Oceanogr.* **27**, 2663–2693.
- LLEWELLYN SMITH, S. G. & YOUNG, W. R. 2003 Tidal conversion at a very steep ridge. *J. Fluid Mech.* **495**, 175–191.
- LODER, J. W. 1980 Topographic rectification of tidal currents on the sides of Georges Bank. *J. Phys. Oceanogr.* **10**, 1399–1416.
- LONGUET-HIGGINS, M. S. 1968 On the trapping of waves along a discontinuity of depth in a rotating ocean. *J. Fluid Mech.* **31** (3), 417–434.
- MAAS, L. R. M. 2011 Topographies lacking tidal conversion. *J. Fluid Mech.* **684**, 5–24.
- MAAS, L. R. M. & ZIMMERMAN, J. T. F. 1989a Tide-topography interactions in a stratified shelf sea. I. Basic equations for quasi-nonlinear internal tides. *Geophys. Astrophys. Fluid Dyn.* **45**, 1–36.
- MAAS, L. R. M. & ZIMMERMAN, J. T. F. 1989b Tide-topography interactions in a stratified shelf sea. II. Bottom trapped internal tides and baroclinic residual currents. *Geophys. Astrophys. Fluid Dyn.* **45**, 37–69.
- MARSHALL, J., ADCROFT, A., HILL, C., PERELMAN, L. & HEISEY, C. 1997 A finite volume, incompressible Navier–Stokes model for studies of the ocean on parallel computers. *J. Geophys. Res.* **102** (C3), 5753–5766.
- MELET, A., VENAYAGAMOORTHY, S. W., LEGG, S. & POLZIN, K. L. 2013 Sensitivity of the ocean state to the vertical distribution of internal-tide-driven mixing. *J. Phys. Oceanogr.* **43** (3), 602–615.
- MÜLLER, M. 2013 On the space-and time-dependence of barotropic-to-baroclinic tidal energy conversion. *Ocean Model.* **72**, 242–252.
- MUNK, W. H. & WUNSCH, C. 1998 Abyssal recipes II: energetics of tidal and wind mixing. *Deep-Sea Res.* I **45** (12), 1977–2010.
- MUSGRAVE, R. C., MACKINNON, J. A., PINKEL, R., WATERHOUSE, A. F. & NASH, J. D. 2016 Tidally driven processes leading to nearfield turbulence in a channel at the crest of the Mendocino Escarpment. *J. Phys. Oceanogr.* (in press).
- NAKAMURA, T., AWAJI, T., HATAYAMA, T., AKITOMO, K., TAKIZAWA, T., KONO, T., KAWASAKI, Y. & FUKASAWA, M. 2000 The generation of large-amplitude unsteady lee waves by subinertial K<sub>1</sub> tidal flow: a possible vertical mixing mechanism in the Kuril Straits. *J. Phys. Oceanogr.* **30** (7), 1601–1621.
- NAKAMURA, T., ISODA, Y., MITSUDERA, H., TAKAGI, S. & NAGASAWA, M. 2010 Breaking of unsteady lee waves generated by diurnal tides. *Geophys. Res. Lett.* **37**, L04602.
- OSAFUNE, S. & YASUDA, I. 2013 Remote impacts of the 18.6 year period modulation of localized tidal mixing in the North Pacific. *J. Geophys. Res.* **118**, 3128–3137.
- PADMAN, L., PLUEDDEMANN, A. J., MUENCH, R. D. & PINKEL, R. 1992 Diurnal tides near the Yermak Plateau. *J. Geophys. Res.* **97** (C8), 12639–12652.

- RAPAKA, N. R., GAYEN, B. & SARKAR, S. 2013 Tidal conversion and turbulence at a model ridge: direct and large eddy simulations. *J. Fluid Mech.* **715**, 181–209.
- RHINES, P. B. 1970 Edge, bottom, and Rossby waves in a rotating stratified fluid. *J. Geophys. Astrophys. Fluid Dyn.* **1** (3–4), 273–302.
- SIMMONS, H. L., JAYNE, S. R., ST LAURENT, L. C. & WEAVER, A. J. 2004 Tidally driven mixing in a numerical model of the ocean general circulation. *Ocean Model.* **6** (3–4), 245–263.
- SMAGORINSKY, J. 1963 General circulation experiments with the primitive equations. *Mon. Weath. Rev.* **91** (3), 99–164.
- ST LAURENT, L. C., STRINGER, S., GARRETT, C. J. R. & PERRAULT-JONCAS, D. 2003 The generation of internal tides at abrupt topography. *Deep-Sea Res. I* **50** (8), 987–1003.
- WINTERS, K. B. & ARMI, L. 2013 The response of a continuously stratified fluid to an oscillating flow past an obstacle. *J. Fluid Mech.* **727**, 83–118.